PSFC/JA-11-12

Investigation of lower hybrid physics through power modulation experiments on Alcator C-Mod

Schmidt, A.E, Bonoli, P.T., Meneghini, O., Parker, R.R., Porkolab, M., Shiraiwa, S., Wallace, G.M., Wright, J.C., Harvey, R.W.*, Wilson, J.R.**

* CompX Co.
** Princeton Plasma Physics Laboratory.

July 2011

**Plasma Science and Fusion Center
Massachusetts Institute of Technology
Cambridge MA 02139 USA**

Investigation of lower hybrid physics through power modulation experiments on Alcator C-Mod

A. E. Schmidt, P. T. Bonoli, O. Meneghini, R. R. Parker, M. Porkolab, S. Shiraiwa, G. Wallace, and J. C. Wright

Massachusetts Institute of Technology Plasma Science and Fusion Center

R. W. Harvey

CompX

J. R. Wilson

Princeton Plasma Physics Laboratory

Lower hybrid current drive (LHCD) is an attractive tool for off-axis current profile control in magneticly confined tokamak plasmas and burning plasmas (ITER), because of its high current drive efficiency. The LHCD system on Alcator C-Mod operates at 4.6 GHz, with ~ 1 MW of coupled power, and can produce a wide range of launched parallel refractive index ($n_{||}$) spectra. A 32 chord, perpendicularly viewing hard x-ray camera has been used to measure the spatial and energy distribution of fast electrons generated by LH waves. Square-wave modulation of LH power on a time scale much faster than the current relaxation time does not significantly alter the poloidal magnetic field inside the plasma and thus allows for realistic modeling and consistent plasma conditions for different $n_{||}$ spectra. Inverted hard x-ray profiles show clear changes in LH-driven fast electron location with differing $n_{||}$. Boxcar binning of hard x-rays during LH power modulation allows for ~ 1 ms time resolution, which is sufficient to resolve the build-up, steady-state, and slowing-down phases of fast electrons. Ray-tracing/Fokker-Planck modeling in combination with a synthetic hard x-ray diagnostic show quantitative agreement with the x-ray data for high $n_{||}$ cases. The time histories of hollow x-ray profiles have been used to measure off-axis fast electron transport in the outer half of the plasma, which is found to be small on a slowing down time scale.

PACS numbers: 52.55.Fa, 52.25.Os, 52.25.Fi, 52.35.Hr

I. INTRODUCTION

Lower hybrid current drive (LHCD) [1–3] is envisioned to be used in advanced tokamak scenarios for both non-inductive current drive and current profile control. The radial location of the fast electrons can be controlled through the launched parallel wave refractive index ($n_{||}$) spectrum, which determines where the wave power damps for a given target plasma. Alcator C-Mod [4] is in a unique position to evaluate the feasibility of LHCD in reactor relevant regimes because it can operate at reactor-relevant densities and magnetic fields, albeit at lower temperatures which may have important implications for electron Landau absorption of the waves. Furthermore, its LH launcher has flexible phasing, allowing for a wide range of launched $n_{||}$, and operates at a similar frequency to what is planned for the ITER LHCD system [5].

Earlier calculations of LH-driven fast electron diffusion coefficients have been deduced from experiments and modeling on Alcator C [6], PBX-M [7], Tore Supra [8, 9], ASDEX [9, 10], and JET [9]. These analyses yielded diffusivities ranging from 0.1 to 10 m^2/s. The wide variety of analysis methods used as well as the wide range of target plasmas contribute to the differences in measured diffusivities on various tokamaks. In each of these previous transport experiments, LH power deposition was primarily in the core, due to the low electron temperatures and/or low launched $n_{||}$. By contrast, the transport coefficients presented in this paper were deduced from hollow, off-axis inverted x-ray profiles, peaked near r/a of 0.7. Thus these measurements of fast electron transport are relevant to LHCD operation in burning plasmas, in which LH power absorption and driven current are expected to be strongly peaked in the outer half of the plasma [5].

The LH power modulation experiments described in this paper led to several results with important implications for LHCD on the next generation of reactors. These experiments showed a clear variation in power deposition location with varying $n_{||}$, a necessary condition for using LHCD as a current profile control tool. A comparison of the resulting hard x-ray (HXR) profiles with the predictions of a synthetic diagnostic [11] from a ray-tracing/Fokker-Planck code showed that the degree to which the experiment and model agreed depended strongly on the launched value of $n_{||}$. Better agreement between modeling and experiment was found for higher values of launched $n_{||}$, where stronger ray damping was apparent in the model. Finally, the time histories of the HXR inverted profiles were used to obtain transport coefficients for fast electrons in the outer half of the plasma. The main conclusion from the transport analysis is that on the slowing down time scale, the fast electrons do not significantly diffuse or convect away from the flux surfaces on which they are born, another necessary condition

for effective current profile control [12].

The outline of this paper is as follows: Section II describes the experimental setup. Section III presents the observed trends in HXR profiles as a function of launched $n_{||}$ and plasma current. Section IV presents accompanying modeling for the $n_{||}$ scan. Section V explains the model used for recovering transport coefficients and reports the measured transport coefficients. Section VI is a summary of the main conclusions drawn from this set of experiments and the accompanying modeling.

II. EXPERIMENTAL SETUP

A. Alcator C-Mod LH system

C-Mod has a 4.6 GHz LHCD system that has coupled up to 1 MW of power into the plasma. The waveguide grill is actively driven with flexible phasing between columns, allowing for a peak of the launched $n_{||}$ spectrum of approximately 1.5 to 3.1. The data presented in this paper span multiple campaigns, during which two generations of LH launchers were used. Both LH launchers were located on the outboard mid-plane. The two launchers had 4 rows by 22 columns and 4 rows by 16 columns of actively driven waveguides, respectively. In the first generation launcher, pairs of columns of waveguides were actively driven by individual klystrons and the phasing between adjacent columns was controlled mechanically. Columns in the (current) second generation launcher are driven the same way, with the exception of the middle 4 columns, which are each individually driven by a single klystron. The second launcher had slightly wider waveguides than the first, allowing for a similar launched $n_{||}$ range with slightly broader spectrum. A picture of the second (current) launcher is shown in Fig. 1.

B. Alcator C-Mod hard x-ray camera

C-Mod has an outboard mid-plane HXR camera with 32 spatial chords, designed to detect bremsstrahlung emission from LH-driven fast electrons [13, 14]. The camera has a spatial resolution of ∼2 cm. It detects single photons in the range of 20-200 keV. Individual photons are time resolved with ∼1 μs accuracy. Flexible time and energy binning can be performed during post-processing.

Figure 2 shows a diagram of the HXR camera. This diagnostic views nearly perpendicularly to the magnetic field and the fast electrons emit bremsstrahlung primarily in the direction of their velocity. A calculation of bremsstrahlung emission from a simulated electron distribution function predicts that the photons detected by the camera originate from fast electrons of many different pitch angles, with comparable emission originating from the forward moving current-carrying electrons and the pitch-angle scattered fast electrons.
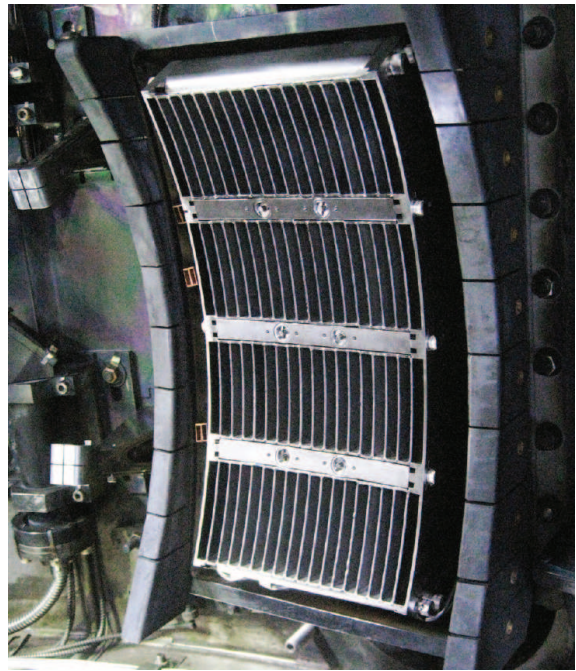

FIG. 1. (Color online) The current installed LH launcher on Alcator C-Mod, with 16 actively driven waveguide columns and 2 passive columns.
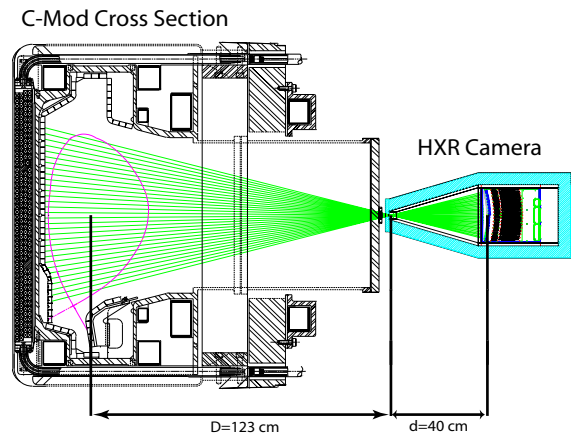

FIG. 2. (Color online) Diagram of the HXR camera and its viewing chords through the C-Mod poloidal cross-section.

C. LH modulation

In the experiments described in this paper, lower hybrid power was square wave modulated with a 25 ms period and a 50% duty cycle, with 20-40 pulses per plasma discharge. The modulation period was chosen to be longer than a typical fast electron slowing down time (about 2 ms for this experiment) and shorter than a current diffusion time (about 100 ms for this experiment). Thus the fast electron distribution function reached a quasi-steady-state before the LH power was turned off. Lower hybrid power was approximately 400
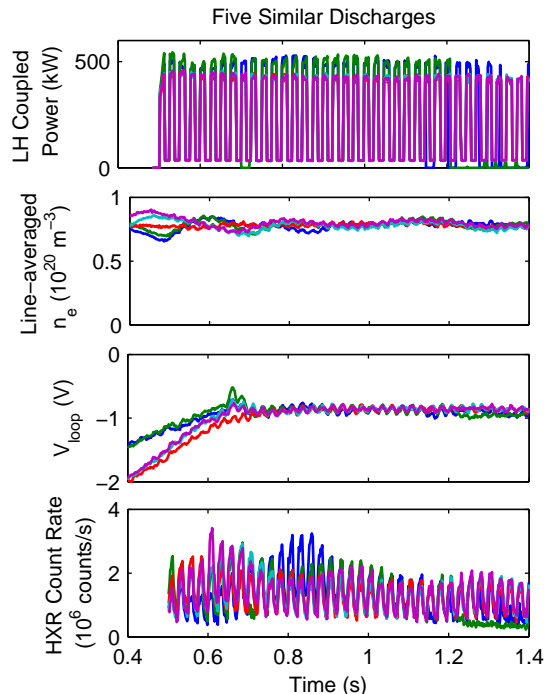
FIG. 3. (Color online) Time traces for 5 similar discharges of experimental parameters: LH coupled power, line-averaged density, loop voltage, and HXR count rates (count rates are summed over all 32 chords for all x-rays 20-200 keV).
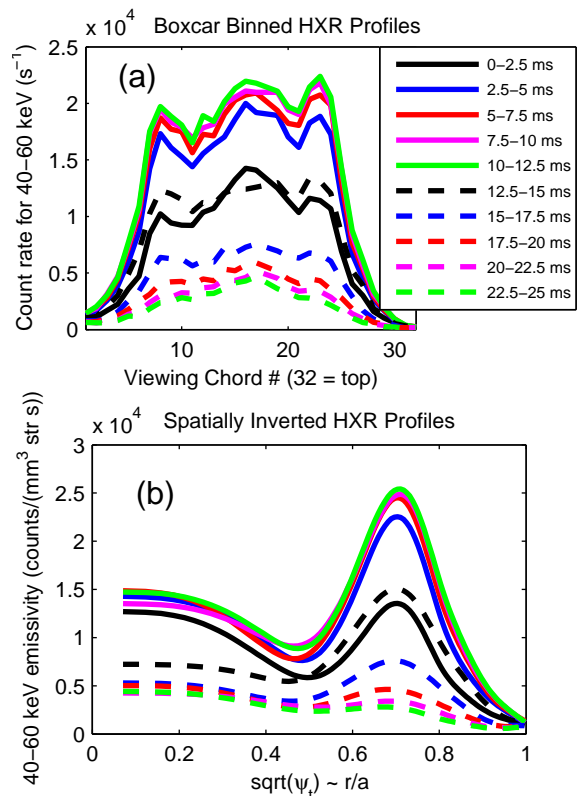

FIG. 4. (Color online) (a) An example of x-ray profiles that have been boxcar binned to obtain high time resolution and (b) inverted x-ray emissivity for the boxcar binned profiles shown in (a). Solid lines indicate times during which the LH power was on and dashed lines indicate times during which LH power was off. The x-ray signal comes to a stable equilibrium at the end of the LH pulse. Plasma parameters for this experiment were B=5.4 T, T_{e0}=2.3 keV, $\bar{n}_e = 9 \times 10^{19}$ m^{-3}, and I_p=800 kA. The peak launched $n_{||}$=3.1 for this case.

kW peak (200 kW time-averaged) for all experiments described here. Loop voltage variation during the experiments did not typically exceed 10% and most of the plasma current was ohmically driven. The launched $n_{||}$ spectrum, the plasma current, and plasma density were held constant for several discharges at each plasma condition. For all experimental results presented in this paper, $\bar{n}_e = 9 \times 10^{19}$ m^{-3} and B=5.4 T. The electron temperature ranges from T_{e0}=1.9-2.3 keV, and will be indicated when results are presented. Figure 3 shows time traces of the LH power, electron density, loop voltage, and HXR count rate for 5 similar discharges.

D.   Boxcar binning

Because the HXR camera detects individual photons, its time resolution is fundamentally limited by count statistics. A typically used x-ray integration time for a moderate density plasma (9×10^{19} m^{-3}) with appreciable steady-state LH power (100s of kW) is 40 ms. In order to time resolve the x-rays during the fast electron tail build up and slowing down, millisecond time resolution is needed. This time resolution is obtained through boxcar binning of the x-rays (averaging over many LH

pulses). Figure 4a shows 10 time traces for Boxcar binned x-rays from a LH modulation experiment with launched $n_{||} = 3.1$, B=5.4 T, T_{e0}=2.3 keV, $\bar{n}_e = 9 \times 10^{19}$ m^{-3}, and I_p=800 kA.

E.   X-ray spatial inversions

Line-integrated x-ray chords can be spatially inverted to obtain emissivity as a function of radius. Inversions are performed using the approximation of constant emissivity on a flux surface. Tikhonov regularization [15] with a second derivative cost function is used to obtain spatially smooth emissivity profiles. Generalized cross validation is used to choose a regularization parameter.

Figure 4b shows inverted x-ray profiles for the boxcar binned x-ray profiles shown in Figure 4a. The high signal-to-noise ratio obtained through boxcar binning allowed for spatial inversions on a fine time scale. Time histories

of inverted profiles can be used to deduce fast electron transport coeffcients, as discussed in Section V.

III. POWER DEPOSITION TRENDS

A. Variation of x-ray profiles with launched spectrum

The main parameter for controlling the driven current location by LHCD is the launched value of $n_{||}$. Quasilinear theory predicts that LH waves will damp when their phase velocity is 2.5 times the electron thermal velocity [16, 17], where $v_{th} = \sqrt{2T_e/m_e}$. This damping condition can alternatively be written as $T_e = (40 \text{ keV})/n_{||}^2$, the electron temperature that the waves must encounter to damp. Thus in a single-pass absorption regime, theory predicts lower $n_{||}$ waves to damp farther in towards the core, where the plasma temperature is higher [16].

However, due to the low temperatures (relative to $40 \text{ keV}/n_{||}^2$) in many present day experiments, LH waves will reflect from the vacuum vessel walls or a cut-off layer at least once before they damp. As the LH wave propagates in the plasma, the $n_{||}$ of the wave can vary due to toroidal effects and the wave does not damp until $n_{||}$ increases enough to damp at the local electron temperature. In these multi-pass absorption regimes, the power damping location depends on the evolution of $n_{||}$ as the wave propagates, not necessarily the launched value. This can be calculated using complex computational tools, such as ray tracing [18, 19] or full-wave [20, 21] codes in toroidal geometry. Ray tracing calculations we have carried out show that in general higher $n_{||}$ waves damp farther off-axis than lower $n_{||}$ waves because they undergo an $n_{||}$ upshift sufficient to damp at lower temperatures.

Hard x-ray data were taken for 3 different values of $n_{||}$: 1.5, 2.3, and 3.1. Figure 5 shows the inverted HXR profiles for these 3 experiments, taken from the last boxcar binned time step during which the LH power was on. In all 3 cases, the peak electron temperature was 2.3 keV, the line-averaged electron density was $9 \times 10^{19} \text{ m}^{-3}$, the plasma current was 800 kA, and the toroidal B field was 5.4 T. The bremsstrahlung emission location indicates that the wave power damps most strongly on axis for the lowest $n_{||}$ case and most strongly off axis for the highest $n_{||}$ case, in qualitative agreement with theory. The fact that power deposition location is strongly dependent on $n_{||}$ indicates that current profile control is attainable with LHCD, using the launched value of $n_{||}$ as a control parameter. The radial dependence on $n_{||}$ of LH power deposition has also been measured on Tore Supra, using real time feedback control of antenna phasing [22].
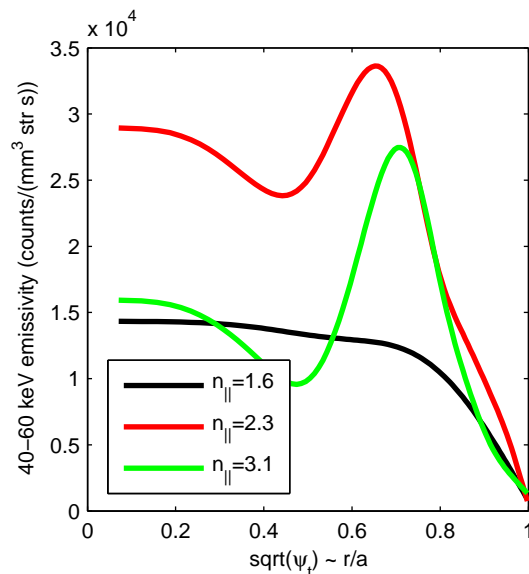
FIG. 5. (Color online) Inverted HXR spectra from discharges with 3 different launched $n_{||}$: 1.6, 2.3, and 3.1. Plasma parameters for this experiment were B=5.4 T, T_{e0}=2.3 keV, $\bar{n}_e = 9 \times 10^{19} \text{ m}^{-3}$, and I_p=800 kA. Inverted profiles have been normalized to $P_{LH}/400$ kW where P_{LH} is the peak LH power in each experiment.
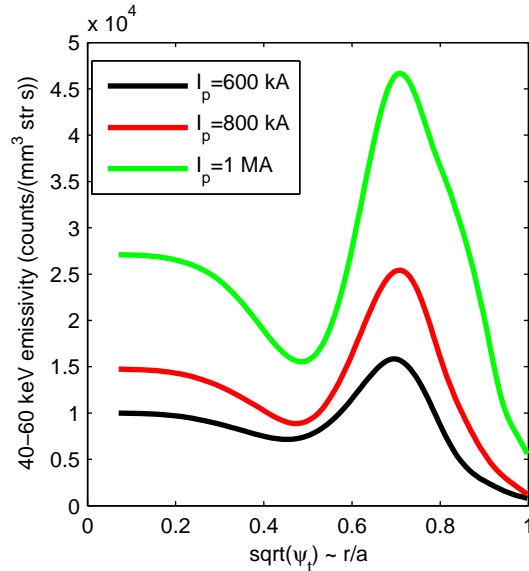
FIG. 6. (Color online) Inverted HXR spectra from discharges with 3 different plasma currents: 600 kA, 800 kA, and 1 MA. Plasma parameters for this experiment were B=5.4 T, $\bar{n}_e = 9 \times 10^{19} \text{ m}^{-3}$. T_{e0} for the 600 kA, 800 kA, and 1 MA discharges was 1.9, 2.3, and 2.1 keV respectively. As the current increased from 600 kA to 1 MA, The loop voltage increased from 0.8 to 1.1 V. The launched $n_{||}$=3.1 for these discharges.

B. Variation of x-ray profiles with plasma current

LH modulation experiments were performed with 3 different plasma currents to examine the dependence of driven fast electron location on plasma current. Figure 6 shows the inverted HXR profiles for these 3 experiments, also taken from the last boxcar binned time step during which the LH power was on. T_{e0} for the 600 kA, 800 kA, and 1 MA discharges was 1.9, 2.3, and 2.1 keV respectively. As the current increased from 600 kA to 1 MA, The loop voltage increased from 0.8 to 1.1 V. For all 3 cases, the peak launched $n_{||}$ was 3.1, the line-averaged electron density was 9×10^{19} m^{-3} and the toroidal B field was 5.4 T. The HXR emission location indicates that the plasma current does not strongly affect the wave power damping location. The x-ray intensity clearly varies for these 3 different scenarios. These variations in flux are likely due to the variation in the DC electric field, which is highest for the 1 MA discharges. However, they could be partially due to differences in the poloidal magnetic field strength as well. Increases in x-ray count rates at higher plasma currents have also been observed on Tore Supra [23].

IV. RAY-TRACING/FOKKER-PLANCK MODELING OF EXPERIMENT

The $n_{||}$ scan discussed in section III A has been modeled using the ray-tracing/Fokker-Planck simulation package Genray [18]/CQL3D [24]. CQL3D contains a synthetic x-ray diagnostic that computes bremsstrahlung emission along a specified line of sight, allowing for direct comparison to experimental x-rays [11]. This provides a stringent benchmarking test for the code and can also aid in interpreting experimental measurements.

The version of Genray used for the modeling shown here did not include a scrape-off-layer (SOL). Rays were allowed to propagate to the last closed flux surface (if they did not encounter a cut-off layer first) before undergoing a specular reflection. In order to ensure that rays reflected from the lower hybrid cut-off layer, as we believe the waves do in the experiment, the plasma density in the model was artificially lowered below the cut-off density inside the separatrix. Rays were launched inside the separatrix in the model.

Each ray in the model is characterized by a poloidal launch location and a launched value of $n_{||}$. The launcher's four waveguide rows are represented in the modeling by four poloidal launch locations, centered at the middle of the waveguides. The $n_{||}$ spectrum is represented in the model by 45 rays (35 in the forward spectrum and 10 in the reverse spectrum) with varying $n_{||}$ at each poloidal launch location. The main forward and main reverse $n_{||}$ lobes are included in the modeling, power scaled appropriately.

A small amount of radial diffusion was included in each simulation. The velocity dependent radial diffusion co-
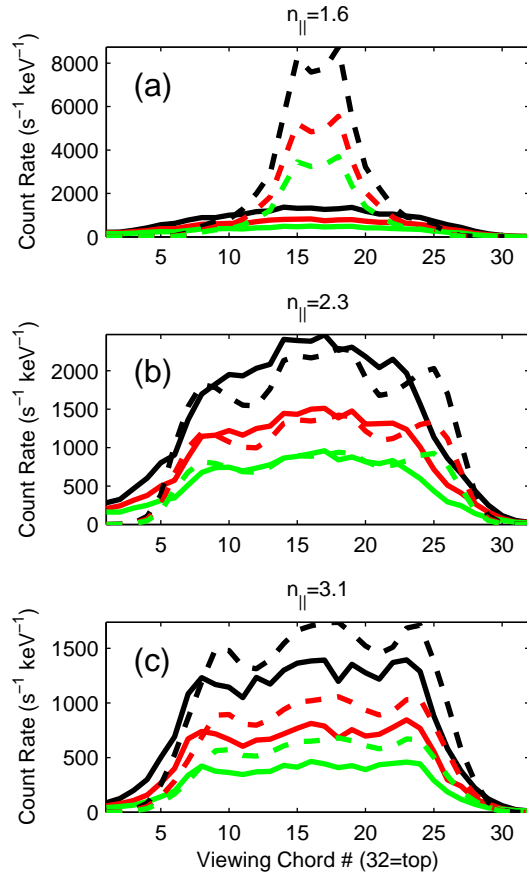

FIG. 7. (Color online) Measured (solid lines) and simulated (dashed lines) x-ray spectra for the (a) launched n$_{||}$=1.6 case, (b) launched n$_{||}$=2.3 case, and (c) launched n$_{||}$=3.1 case. Three different x-ray energies are shown: (black) 45 keV, (red/dark grey) 55 keV, and (green/light grey) 65 keV. Plasma parameters for this experiment were B=5.4 T, T$_{e0}$=2.3 keV, $\bar{n}_e = 9 \times 10^{19}$ m^{-3}, and I$_p$=800 kA. A fast electron spatial diffusion coefficient of $.01v_{||}/(v_{th}\gamma^3)$ m^2/s was used in each simulation.

efficient used was $.01v_{||}/(v_{th}\gamma^3)$ m^2/s, where γ is the relativistic factor. This scaling is based on a magnetic turbulence model [25].

Figure 7 shows the simulated and experimental hard x-ray profiles for $n_{||}$=1.6, 2.3, and 3.1. Figure 8 shows the simulated power density profiles, which can be qualitatively compared with the inverted HXR profiles in Figure 5.

It is clear that the poorest agreement is obtained in the $n_{||} = 1.6$ case, where the simulation predicts that the power damps predominantly on axis but the experimental x-rays are much broader. The best qualitative agreement between inverted experimental HXR profiles and simulated power density profiles is obtained in the $n_{||} = 3.1$ case, where the power deposition is mainly in a single peak, located radially near the peak in the inverted
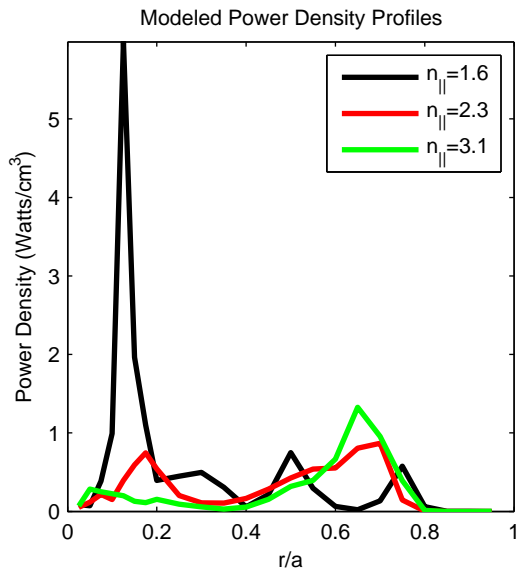
FIG. 8. (Color online) Simulated power density profiles, for qualitative comparison with the inverted experimental HXR shown in Figure 5. The best qualitative agreement is obtained in the $n_{||}$=3.1 simulation, where the simulated power deposition is peaked off-axis at r/a=0.65.
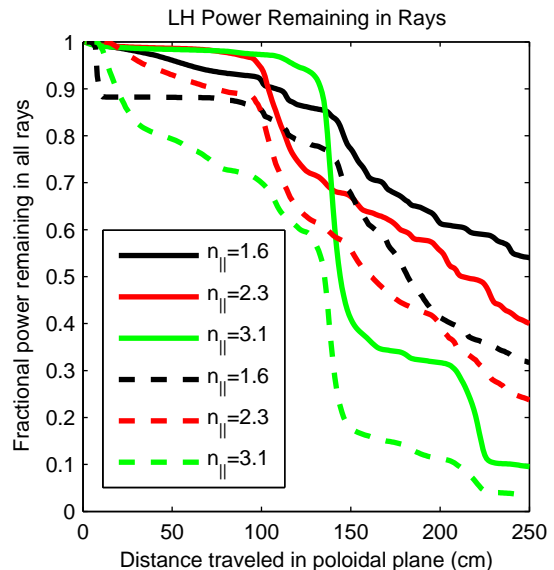

FIG. 9. (Color online) Fractional power remaining in all rays representing the forward wave spectrum as a function of poloidal distance traveled in the plasma for 3 different antenna phasings. Solid lines show power remaining when rays are damped on a thermal (Maxwellian) plasma. Dashed lines show power remaining when rays are damped on a non-thermal distribution function, during the last iteration between Genray and CQL3D.

HXR in Figure 5.

The authors attribute the poor agreement for the low $n_{||}$ case to the multiple passes that the rays undergo before they damp because the initial parallel phase velocity of the wave is very large compared to the electron thermal velocity. This idea can be further explored by looking at the ray power damping in each case.

Figure 9 shows the fraction of power remaining in all rays representing the forward wave spectrum as a function of poloidal distance traveled in the plasma for the 3 different antenna phasings modeled. The fractional wave power is shown for waves damping on a Maxwellian electron distribution (the first iteration of Genray) and on a non-thermal electron tail (the last iteration of Genray).

It is clear from Figure 9 that the rays damp most strongly in the $n_{||}$ = 3.1 case and most weakly in the $n_{||}$ = 1.6 case, regardless of whether they are damping on a Maxwellian plasma or a non-thermal plasma. In particular, the rays for the $n_{||}$=1.6 case damp very weakly in the first 100-150 cm of poloidal propagation distance, where the rays undergo their first few reflections. Because ray tracing is an initial value problem, we would expect the code's predictions to be least accurate in cases where many passes of the rays are necessary for the rays to damp. In particular, the ray paths and $n_{||}$ can be modified significantly at or near reflections, in a region of the plasma (the SOL) that is not being modeled. Significant modification of the LH wave front can also occur at cut-offs due to full-wave effects such as diffraction and scattering that are not included in the ray tracing.

It is important for accurate predictions that the waves damp significantly in a minimal number of passes on both

the Maxwellian plasma and the non-thermal plasma. Ray damping on a Maxwellian plasma during the first iteration of Genray seeds the fast electron population in a particular radial location. Ray damping during subsequent iterations with Genray tend to be strongest in radial locations where a fast electron tail has already been populated from previous iterations, though a flattening of the distribution function from quasilinear saturation can also have the effect of decreasing local Landau damping.

While the approximation of moving the cut-off layer inside the separatrix appears to be valid for the two higher $n_{||}$ cases, where not as many ray passes are needed for damping, it may not be sufficient for modeling the lowest $n_{||}$ case. In this case, ray tracing with a SOL model or full-wave model might more accurately predict the wave damping. Since it is expected that LH waves will exhibit single pass absorption in at reactor relevant temperatures, modeling presented here suggests that ray-tracing/Fokker-Planck may be valid in temperature regimes relevant to ITER, at least at the plasma densities used here.

V. TRANSPORT MEASUREMENTS

It is a necessary condition for current profile control that fast electrons remain near the radial location on which they are born until they thermalize. Furthermore, transport of fast electrons to the wall could potentially

be damaging to plasma facing components. To that end, the LH modulation experiments were designed to quantify off-axis fast electron transport. Convection velocities and diffusivities of fast electrons have been deduced from off-axis (hollow) HXR emissivity profiles. Convection and diffusion have been found to be small on a fast electron slowing down time scale, so that current profile control is maintained.

A. Transport model and assumptions

The HXR data from the LH modulation experiments can be fit to a transport model in order to solve for a slowing down time, a diffusivity, and a convective velocity. Let $n(r,t)$ be a fast electron number density. The x-ray emissivity (and therefore also the spatially inverted HXR signal) is proportional to $n(r,t)n_e(r)$, where $n_e(r)$ is the bulk electron density profile, so that $n(r,t)$ can be obtained from the inverted HXR signals simply by dividing by the bulk density profile.

We propose that $n(r,t)$ obeys the model transport Eq. 1,

$$\frac{\partial n}{\partial t} = -\frac{n}{\tau} - \nabla \cdot (nv) + \nabla \cdot (D\nabla n) + S(r,t), \quad (1)$$

where τ is a slowing-down time, D is a spatial diffusion coefficient, v is a convection velocity, and S is a source of fast electrons.

Because the LH modulation experiments are periodic, $n(r,t)$ can be decomposed into its Fourier components, as shown in Eq. 2, where ω is the experimental modulation frequency.

$$n(r,t) = n_0(r,t) + n_{1i}(r)\sin(\omega t) + n_{3i}(r)\sin(3\omega t) + \ldots$$
$$+ n_{1r}(r)\cos(\omega t) + n_{3r}(r)\cos(3\omega t) + \ldots (2)$$

The fast electron source term, $S(r,t)$, is assumed to be proportional to the LH power time trace (an odd function in time):

$$S(r,t) = S(r)[Const. + \sin(\omega(t)) + \frac{1}{3}\sin(3\omega(t)) + \ldots]. \quad (3)$$

Furthermore, it is assumed that τ is inversely proportional to the local bulk electron density:

$$\tau(r) = \frac{\tau(r_{peak})n_e(r_{peak})}{n_e(r)}, \quad (4)$$

where r_{peak} is the radial location of the HXR emissivity peak, and $\tau(r_{peak})$ and $n_e(r_{peak})$ are the slowing down time and electron density at r_{peak}, respectively.

Equations. 2, 3, and 4 can be substituted into Eq. 1, resulting in a series of sine and cosine terms. Collecting $\cos(\omega t)$ terms yields the relation:
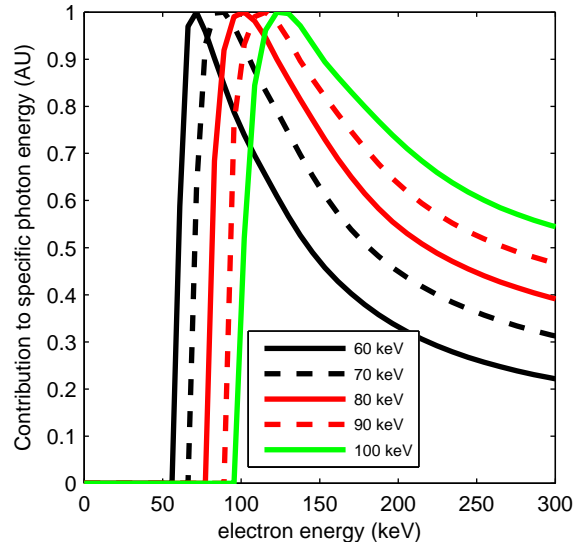

FIG. 10. (Color online) Normalized contribution of various electron energies to a specific photon energy, based on bremsstrahlung cross-sections and a simulated electron distribution function.

$$\omega n_{1i}(r) = -\frac{n_{1r}(r)n_e(r)}{\tau(r_{peak})n_e(r_{peak})} - \nabla \cdot [n_{1r}(r)\mathbf{v}] + \nabla \cdot (D\nabla n_{1r}(r)), \quad (5)$$

where $n_{1r}(r)$ and $n_{1i}(r)$ are the real and imaginary fundamental frequency Fourier components of the inverted HXR profiles from Eq. 2. The unknown source term is eliminated in the cosine component. Higher order cosine terms are not used in the analysis due to poor signal-to-noise.

Equation 5 relates $n_{1i}(r)$ to $n_{1r}(r)$ and its spatial derivatives. The free parameters $\tau(r_{peak})$, v, and D can be determined such that the left and right sides of Eq. 5 are equal in magnitude and first and second derivatives at a local peak in the profile. Physically, the $n_{1i}(r)$ term originates from a direct response to the (odd in time) drive and the $n_{1r}(r)$ term corresponds to a phase-lagged response. Thus the ratio of the magnitude of the two peaks is a measure of the time response of the system (the slowing down time). Differences in peak location can be attributed to convection, while differences in peak width can be attributed to diffusion.

This analysis can be performed for several photon energy bins, effectively allowing us to see how transport coefficients trend with electron energy. It is important to remember that photons of any given energy may originate from a wide range of electron energies. Thus the measured transport coefficients are "effective" velocities and diffusivities of electrons that contribute to a particular photon energy.

Figure 10 shows the weighted contribution of various electron energies to specific photon energies, based on
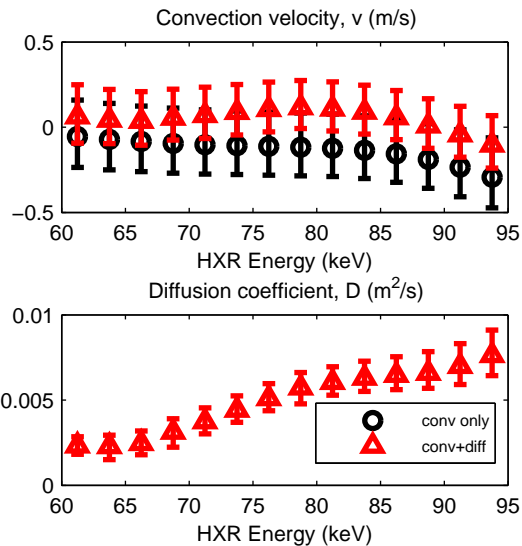
FIG. 11. (Color online) Inferred fast electron convection velocities and diffusivities for the I_p=800 kA case discussed in section III B. In this case, the launched $n_{||}$=3.1. Plasma parameters were B=5.4 T, T_{e0}=2.3 keV, and $\bar{n}_e = 9 \times 10^{19}$ m^{-3}.

FIG. 12. (Color online) Inferred fast electron convection velocities and diffusivities for the I_p=600 kA case discussed in section III B. In this case, the launched $n_{||}$=3.1. Plasma parameters were B=5.4 T, T_{e0}=1.9 keV, and $\bar{n}_e = 9 \times 10^{19}$ m^{-3}. In this case, convection and diffusion were included in the model one at a time.

a convolution of bremsstrahlung cross-sections [26] with the electron distribution function produced by the modeling in section IV. It is clear from Fig. 10 that photons of a given energy originate from a wide range of electron energies, though electrons at slightly above the given photon energy contribute the most photon flux.

B. Convection and diffusion measurements

The model described in Section V A was used to solve for convection velocities and diffusivities for the hollow x-ray profiles produced by the $n_{||}$=3.1 cases, at plasma currents of 600 kA and 800 kA.

Figure 11 shows the measured convection velocities and diffusivities for fast electrons emitting at various photon energies for the 800 kA plasma current case discussed in section III B. The convection velocities were calculated using two different models. In one model, convection was the only transport mechanism. The second model included both convection and diffusion.

The measured convection is small – zero within error bars for most energies. The measured diffusivities are also small, all $D \leq$.01 m^2/s. Typical measured slowing down times (not shown) for this case are 3 ms. With an upper bound of $|v| \leq$0.5 m/s on convection and $D \leq$.01 m^2/s on diffusion, a fast electron could convect or diffuse a maximum of 2 mm or 5 mm respectively on a slowing down time scale. These are relatively small displacements for C-Mod, whose minor radius is 23 cm.

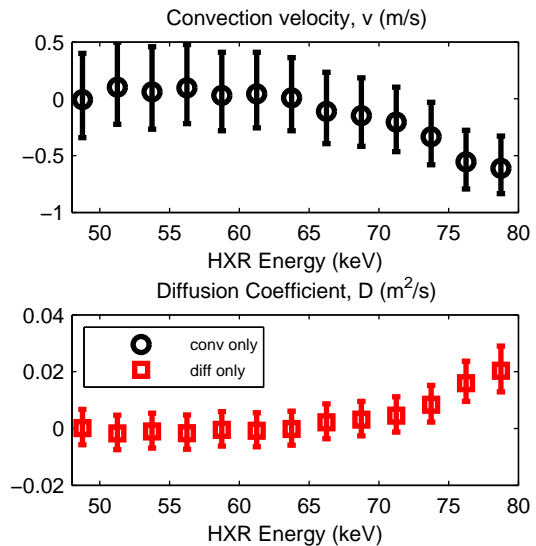Figure 12 shows the measured convection velocities and diffusivities for fast electrons emitting at various photon

energies for the 600 kA plasma current case discussed in section III B. In this case, the model was unable to distinguish between the effects of convection and diffusion. As a result, the two quantities were not solved for simultaneously. Instead, one model excludes diffusion and calculates convection, while the other excludes convection and calculates diffusion.

As in the previous case, the measured convection and diffusion are small. Typical measured slowing down times (not shown) for this case are 2 ms. With an upper bound of 1 m/s on convection and .02 m^2/s on diffusion, a fast electron could convect or diffuse a maximum of 2 mm or 6 mm respectively on a slowing down time scale.

VI. CONCLUSION

The lower hybrid power modulation experiments on Alcator C-Mod led to several interesting physics results. Boxcar binning of the resultant HXR signal produced high signal-to-noise x-ray profiles that are well resolved in time. An $n_{||}$ scan showed clear variation in power deposition location with launched spectrum, in agreement with theoretical expectations. A current scan showed little variation in power deposition location with changes in plasma current. Modeling of the line-integrated HXR count rates with a combined ray-tracing/Fokker-Planck code showed that agreement with experiment for high $n_{||}$ launched rays was excellent. Agreement for the lowest $n_{||}$ case, in which rays undergo many radial reflections at the plasma edge, was significantly poorer. A simple trans-

port model has been used to determine upper bounds on fast electron transport of $D \leq .02m^2/s, |v| \leq .75m/s$, indicating that fast electrons do not stray far from the flux surface where they are born before slowing down.

The results presented in this paper are encouraging for the use of LHCD on the next generation of tokamaks, which are expected to operate at higher electron temperatures. The variation in bremsstrahlung emission location based on the launched $n_{||}$ spectrum implies that LH power deposition location can be controlled through antenna phasing. The small magnitude of diffusion and convection in the outer half of the plasma suggests that the LH-driven fast electrons remain localized. The combination of these two results indicates that LHCD may be used effectively for current profile control in the next generation of reactors. Furthermore, this analysis was the first of its kind to be performed at reactor-relevant densities and magnetic fields with LH power deposition dominantly in the outer half of the plasma.

The agreement between experimental measurements and the synthetic x-ray diagnostic for moderate-to-strong damping cases is encouraging evidence that ray-tracing/Fokker-Plank modeling has strong predictive power for the next generation of tokamaks, where strong single-pass damping of the waves is expected due to higher electron temperatures. In particular, it may be very useful for simulating LHCD scenarios on ITER.

[1] N. J. Fisch, Phys. Rev. Lett. **41**, 873 (1978).
[2] N. J. Fisch and A. H. Boozer, Phys. Rev. Lett. **45**, 720 (1980).
[3] N. J. Fisch, Reviews of Modern Physics **59**, 175 (1987).
[4] I. H. Hutchinson, R. Boivin, F. Bombarda, P. Bonoli, S. Fairfax, C. Fiore, J. Goetz, S. Golovato, R. Granetz, M. Greenwald, *et al.*, Phys. Plasmas **1**, 1511 (1994).
[5] G. Hoang, A. Bécoulet, J. Jacquinot, J. Artaud, Y. Bae, B. Beaumont, J. Belo, G. Berger-By, J. P. Bizarro, P. Bonoli, *et al.*, Nuclear Fusion **49**, 075001 (2009).
[6] S. Knowlton, M. Porkolab, and Y. Takase, Phys. Plasmas **1**, 891 (1994).
[7] S. E. Jones, J. Kesner, S. Luckhardt, F. Paoletti, S. von Goeler, S. Bernabei, R. Kaita, PBX-M Team, and G. Giruzzi, Phys. Plasmas **2**, 1548 (1995).
[8] D. Moreau and the TORE SUPRA Team, Physics of Fluids B: Plasma Physics **4**, 2165 (1992).
[9] Y. Peysson, Plasma Physics and Controlled Fusion **35**, B253 (1993).
[10] R. Bartiromo, E. Barbato, L. Gabellieri, A. Spaziani, A. Tuccillo, F. Leuterer, F. Soldner, O. Gehre, and H. Murmann, Nuclear Fusion **33**, 1483 (1993).
[11] R. Harvey, *X-Ray Energy Spectra Calculated from CQL3D Fokker-Planck Electron Distributions*, Tech. Rep. (CompX, Del Mar, CA report CompX-2000-2, 2000).
[12] J. Rax and D. Moreau, Nuclear Fusion **29**, 1751 (1989).
[13] J. Liptac, R. Parker, V. Tang, Y. Peysson, and J. Decker, Review of Scientific Instruments **77**, 103504 (2006).
[14] J. Liptac, Ph.D. thesis, Massachusetts Institute of Technology (2006).
[15] A. N. Tikhonov and V. Y. Arsenin, *Solutions of Ill-Posed Problems*, edited by F. John (V. H. Winston and Sons, Washington, D.C., 1977).
[16] M. Brambilla, Proc. Physics of Plasmas Close to Thermonuclear Conditions, Varenna, Italy, 1979, edited by C.E.C. (Brussels, 1980), **I**, p. 291.
[17] P. T. Bonoli and R. C. Englade, Physics of Fluids **29**, 2937 (1986).
[18] A. P. Smirnov and R. Harvey, Bull. Am. Phys. Soc. **40** (1995).
[19] Y. Peysson and J. Decker, *C3PO, a ray-tracing code for arbitrary axisymmetric magnetic equilibrium*, Tech. Rep. (Report EUR-CEA-FC-1739, Euratom-CEA, 2008).
[20] J. C. Wright, P. T. Bonoli, A. E. Schmidt, C. K. Phillips, E. J. Valeo, R. W. Harvey, and M. A. Brambilla, Phys. Plasmas **16**, 072502 (2009).
[21] S. Shiraiwa, O. Meneghini, R. Parker, P. Bonoli, M. Garrett, M. C. Kaufman, J. C. Wright, and S. Wukitch, Phys. Plasmas **17**, 056119 (2010).
[22] O. Barana, D. Mazon, L. Laborde, and F. Turco, Plasma Physics and Controlled Fusion **49**, 947 (2007).
[23] Y. Peysson and the TORE SUPRA Team, Plasma Physics and Controlled Fusion **42**, B87 (2000).
[24] R. W. Harvey and M. G. McCoy, Proceedings of the IAEA Technical Committee Meeting on Simulation and Modeling of Thermonuclear Plasmas [Available through USDOC/NTIS No. DE93002962, and www.compxco.com/cql3d] (1992).
[25] H. E. Mynick and J. D. Strachan, Physics of Fluids **24**, 695 (1981).
[26] H. W. Koch and J. W. Motz, Reviews of Modern Physics **31**, 920 (1959).